

Engineering exotic second-order topological semimetals by periodic driving

Bao-Qin Wang,^{1,*} Hong Wu,^{1,*} and Jun-Hong An^{1,†}

¹Lanzhou Center for Theoretical Physics, Key Laboratory of Theoretical Physics of Gansu Province, Lanzhou University, Lanzhou 730000, China

Second-order topological semimetals (SOTSMs) are featured with hinge Fermi arcs. How to generate them in different systems has attracted much attention. We propose a scheme to create exotic SOTSMs by periodic driving. Novel Dirac SOTSMs, with a widely tunable number of nodes and hinge Fermi arcs, the adjacent nodes having the same chirality, and the coexisting nodal points and loops, are generated at ease by the periodic driving. When the time-reversal symmetry is broken, our scheme permits us to realize hybrid-order Weyl semimetals with the coexisting hinge and surface Fermi arcs. Our Weyl semimetals possess a rich hybrid of 2D sliced zero- and π/T -mode topological phases, which may be any combination of the normal insulator, Chern insulator, and second-order topological insulator. Enriching the family of topological semimetals, our scheme supplies a convenient way to artificially synthesize exotic topological phases by periodic driving.

I. INTRODUCTION

Topological quantum matters [1–5] including topological insulator, superconductor, and semimetal enrich the paradigm of condensed matter physics. The finding of higher-order topological phases opens up a new frontier of topological physics [6–19]. Featured with hinge and corner states for three (3D)- and two-dimensional (2D) systems, second-order topological insulators (SOTIs) with some fantastic applications [20] have been realized in various systems [21–30]. On the other hand, topological Dirac [31–39] and Weyl [40–54] semimetals also have been widely studied due to their chiral anomaly and close connection with diverse topological phases [54–59]. Second-order topological semimetals (SOTSMs) in both Dirac [60–64] and Weyl types [65, 66] were recently proposed. Different from surface Fermi arc in first-order semimetals, SOTSMs manifest in hinge Fermi arc [64–66]. Although they have been simulated in classical acoustic metamaterials [67, 68], their observation of SOTSMs in electronic materials is hard. One of the difficulties is that the control ways to various of interactions in natural materials are limited because their features would not be switched once they are fabricated.

Coherent control via periodic driving dubbed Floquet engineering has become a versatile tool in creating topological phases in systems of ultracold atoms [69, 70], photonics [71, 72], superconductor qubits [73], and graphene [74]. It permits us to artificially synthesize a variety of exotic topological phases [75–79]. Greatly increasing the controllability and reducing the realistic difficulty in generating topological phases by adjusting intrinsic parameters of static systems, Floquet engineering supplies an extra dimension in exploring topological matters. Following the theme of condensed-matter physics in discovering novel quantum matter, one generally desires to know what exotic features can be created in the

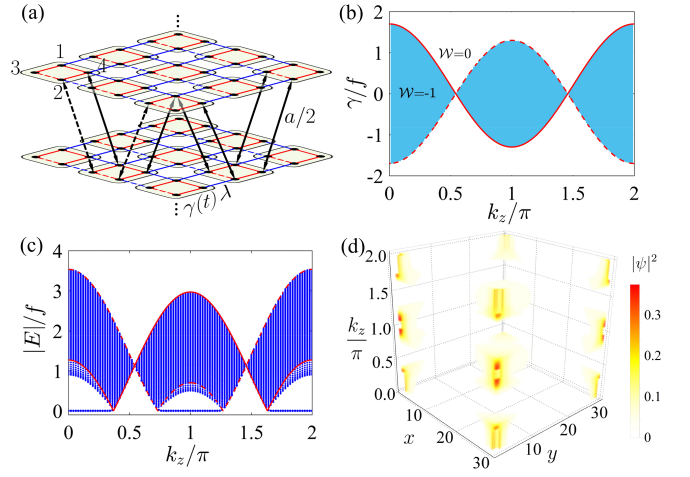


FIG. 1. (a) Schematics of SOTSM on a cubic lattice with an intracell hopping rate γ , and intercell ones λ in the single layer and $a/2$ between two neighboring layers, respectively. The dashed lines denote the hopping rates with a π -phase difference from their solid counterparts. (b) Static phase diagram described by the winding number \mathcal{W} . (c) Energy spectrum and (d) hinge Fermi arcs under the x, y -direction open boundary condition when $\gamma = 0.8f$. The red solid (dashed) lines in (b) and (c) are the dispersion relations of $\theta = \pi$ (0). We use $\lambda = 0.2f$, $a = 1.5f$, and the lattice numbers $L_x = L_y = 30$.

recently proposed SOTSMs by this novel dimension. Further, one also expects Floquet engineering to enrich the control way to complicated interactions in natural materials such that the difficulty in observing SOTSMs there could be reduced. Although some studies on Floquet engineering to SOTIs have been performed [80–89], those for SOTSMs are still lacking. A challenge is how to establish the bulk-corner correspondence (BCC) under the fact that the periodic-driving induced symmetry breaking and the presence of novel π/T -mode corner states invalidates the BCC of the original static system.

We propose a scheme to artificially create exotic SOTSMs by Floquet engineering. A complete BCC to the SOTSMs induced by periodic driving is estab-

* These two authors contributed equally.

† anjhong@lzu.edu.cn

lished. Taking a system of spinless fermions moving on a cubic lattice as an example, we find diverse Dirac SOTSMs with a widely tunable number of nodes and hinge Fermi arcs, the adjacent nodes appearing in pair of same chirality, and the coexisting second-order nodal points and lines, which are absent in the static system. By adding a perturbation to break the time-reversal symmetry, hybrid-order Weyl SOTSMs manifesting in the coexisting hinge and surface Fermi arcs are created by the driving. Our work highlights Floquet engineering as a convenient way to control and explore novel SOTSMs.

II. STATIC SYSTEM

We investigate a system of spinless fermions moving on a 3D lattice [see Fig. 1(a)]. Its Hamiltonian [90] reads $\hat{H} = \sum_{\mathbf{k}} \hat{\mathbf{C}}_{\mathbf{k}}^\dagger \mathcal{H}(\mathbf{k}) \hat{\mathbf{C}}_{\mathbf{k}}$, with $\hat{\mathbf{C}}_{\mathbf{k}}^\dagger = (\hat{c}_{\mathbf{k},1}^\dagger \ \hat{c}_{\mathbf{k},2}^\dagger \ \hat{c}_{\mathbf{k},3}^\dagger \ \hat{c}_{\mathbf{k},4}^\dagger)$ and [6]

$$\mathcal{H}(\mathbf{k}) = [\gamma + \chi(k_z) \cos k_x] \Gamma_5 - \chi(k_z) \sin k_x \Gamma_3 \\ - [\gamma + \chi(k_z) \cos k_y] \Gamma_2 - \chi(k_z) \sin k_y \Gamma_1, \quad (1)$$

where λ , γ , and a are, respectively, the intercell, intracell, and interlayer hopping rates, $\chi(k_z) = \lambda + a \cos k_z$, $\Gamma_{1/2/3} = \tau_y \sigma_{x/y/z}$, $\Gamma_4 = \tau_z \sigma_0$, and $\Gamma_5 = \tau_x \sigma_0$, with τ_i and σ_i being Pauli matrices, τ_0 and σ_0 being identity matrices. It is a 3D generalization of 2D SOTIs in the Benalcazar-Bernevig-Hughes model [91] by considering the interlayer hopping. It is different from the one of Ref. [66] only in the interlayer-hopping way.

The SOTSM is sliced into a family of 2D k_z -dependent SOTIs and normal insulators. As a prerequisite for Dirac semimetal, the time-reversal $\mathcal{T} = K$, with K being the complex conjugation, and inversion $\mathcal{P} = \tau_0 \sigma_y$ symmetries are respected. The system also has the mirror-rotation $\mathcal{M}_{xy} = [(\tau_0 - \tau_z) \sigma_x - (\tau_0 + \tau_z) \sigma_z]/2$ and chiral $\mathcal{S} = \tau_z \sigma_0$ symmetries. Thus, the 2D SOTIs are well described by $\mathcal{H}(\theta, \theta, k_z)$ along the high-symmetry line $k_x = k_y \equiv \theta$, which is diagonalized into $\text{diag}[\mathcal{H}^+(\theta, k_z), \mathcal{H}^-(\theta, k_z)]$ with $\mathcal{H}^\pm(\theta, k_z) = \mathbf{h}^\pm \cdot \boldsymbol{\sigma}$ and $\mathbf{h}^\pm = \sqrt{2}[\gamma + \chi(k_z) \cos \theta, \pm \chi(k_z) \sin \theta, 0]$. Its topology is characterized by the mirror-graded winding numbers $\mathcal{W}(k_z) = (\mathcal{W}_+ - \mathcal{W}_-)/2$, where \mathcal{W}_\pm are the winding numbers of $\mathcal{H}^\pm(\theta, k_z)$ [24, 90]. The phase diagram in Fig. 1(b) reveals a phase transition at $|\gamma| = |\chi(k_z)|$, where $\mathcal{W}(k_z) = -1$ signifies the formation of a SOTI. The energy spectrum in Fig. 1(c) confirms the presence of a $4|\mathcal{W}(k_z)|$ -fold degenerate zero-mode state distributing at the corners. The corner state contributes to the hinge Fermi arcs [see Fig. 1(d)]. The family of 2D SOTIs forms a 3D SOTSM which hosts the Dirac nodes at the critical points $k_z = \arccos[-(\lambda \pm \gamma)/a]$ of 2D SOTI transition. Each Dirac node carries a chirality \mathcal{Q} [55]. The chirality of the Dirac node $k_{z,0}$ equals to the difference of the winding numbers of its separated phases, i.e., $\mathcal{Q} = \mathcal{W}(k_{z,0} + \delta) - \mathcal{W}(k_{z,0} - \delta)$, with $\delta > 0$ being an infinitesimal [90]. Figure 1(b) shows the adjacent Dirac

nodes have the opposite \mathcal{Q} , which explains that only one four-fold degenerate corner state at most is formed.

III. PERIODIC-DRIVING INDUCED EXOTIC SOTSMs

A. Dirac SOTSMs via Floquet engineering

We consider that the intracell hopping γ periodically changes its strength in a step-like manner within the respective time duration T_1 and T_2 as

$$\gamma(t) = \begin{cases} \gamma_1 = q_1 f, & t \in [mT, mT + T_1) \\ \gamma_2 = q_2 f, & t \in [mT + T_1, (m+1)T), \end{cases} \quad (2)$$

where $m \in \mathbb{Z}$, $T = T_1 + T_2$ is the driving period, and f is an energy scale to make the amplitudes q_j dimensionless. Determined by the overlap of spatial wave-function of the fermion on the relevant sites, $\gamma(t)$ could be realized by applying electric field via gate voltage. A periodic system $\hat{H}(t)$ does not have well-defined energies. According to Floquet theorem, the one-period evolution operator $\hat{U}_T = \mathbb{T} e^{-i \int_0^T \hat{H}(t) dt}$ defines an effective Hamiltonian $\hat{H}_{\text{eff}} \equiv \frac{i}{T} \ln \hat{U}_T$ whose eigenvalues are called the quasienergies [92, 93]. The SOTSMs of our periodic system are defined in such quasienergy spectrum. Applying Floquet theorem on a general four-band $\mathcal{H}_j(\mathbf{k}) = \mathbf{n}_j \cdot \boldsymbol{\Gamma}$, we have $\mathcal{H}_{\text{eff}}(\mathbf{k}) = \frac{i}{T} \ln[e^{-i \mathcal{H}_2(\mathbf{k}) T_2} e^{-i \mathcal{H}_1(\mathbf{k}) T_1}]$ [90]. First, we obtain from $\mathcal{H}_{\text{eff}}(\mathbf{k})$ that the bands close for \mathbf{k} and driving parameters satisfying either

$$T_j E_j = z_j \pi, \quad (3)$$

$$\text{or } \begin{cases} \mathbf{n}_1 \cdot \mathbf{n}_2 = \pm 1, \\ T_1 E_1 \pm T_2 E_2 = z \pi, \end{cases} \quad (4)$$

with $\mathbf{n}_j \equiv \mathbf{n}_j/|\mathbf{n}_j|$, at the quasienergy zero (or π/T) when z_j are integers with same (or different) parities and z is even (or odd) number. Giving the positions of Dirac nodes, Eqs. (3) and (4) provide a guideline to control the driving parameters for engineering various Dirac nodes at will. Deriving \mathbf{n}_j from Eq. (1) with γ driven as Eq. (2), we obtain the conditions for the Dirac nodes as follows. **Case I:** Equation (3) results in that the Dirac nodes present at \mathbf{k} satisfying

$$\sqrt{2}[\gamma_j^2 + \chi^2(k_z) + \gamma_j \chi(k_z)(\cos k_x + \cos k_y)]^{\frac{1}{2}} T_j = z_j \pi. \quad (5)$$

Satisfied by three independent parameters (k_x, k_y, k_z) , the two constraints in Eqs. (5) result in the band-touching points to form a loop instead of discrete points. Thus, it generally gives a nodal-line semimetal. Defined in the full Brillouin zone (BZ), Eqs. (5) describe the physics beyond the high-symmetry lines.

Case II: $\mathbf{n}_1 \cdot \mathbf{n}_2 = \pm 1$ needs the high-symmetry line $\theta = 0$ or π . According to Eq. (4), the Dirac nodes present when

$$\sqrt{2}[\gamma_1 + \chi(k_z) e^{i\theta} |T_1 \pm \gamma_2 + \chi(k_z) e^{i\theta} |T_2] = z_{\theta, \pm} \pi, \quad (6)$$

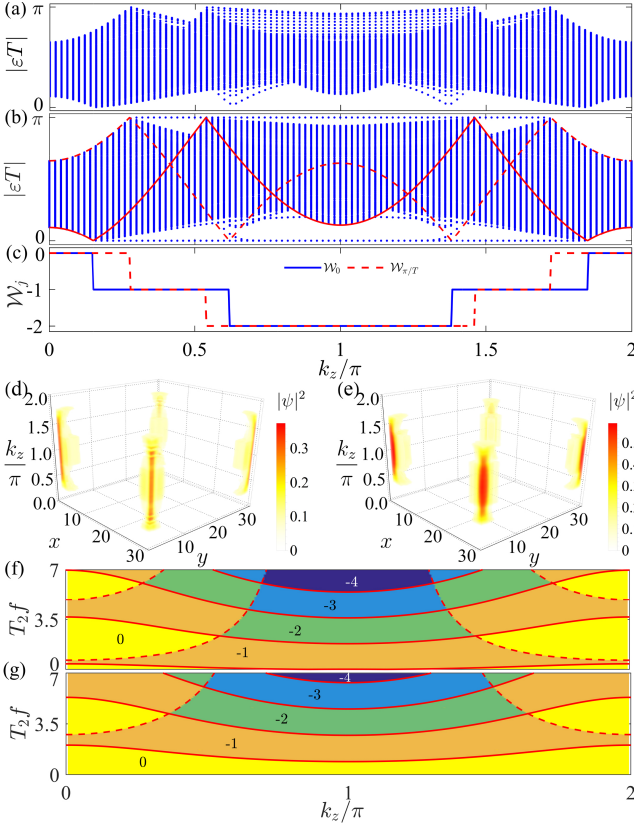


FIG. 2. Quasienergy spectra as the change of k_z under x - (a) and x, y -direction (b) open boundary conditions. The red solid (dashed) line is the dispersion relation along the high-symmetry line $\theta = \pi$ (0). (c) Mirror-graded winding numbers for the zero- and π/T -mode corner states as the change of k_z . Hinge Fermi arcs contributed by the zero- (d) and π/T -mode (e) corner states. Phase diagram characterized by \mathcal{W}_0 (f) and $\mathcal{W}_{\pi/T}$ (g). Phase boundaries obtained from Eq. (6) with $z_{\pi,-} = 0, -2, -4$, and -6 in (f) and $-1, -3, -5$, and -7 in (g) by solid lines and with $z_{0,-} = 0$ and -2 in (f) and -1 in (g) by dashed lines. We use $T_1 = 0.5f^{-1}$, $T_2 = 3.5f^{-1}$, $q_2 = -q_1 = 1.2$, $\lambda = -0.7f$, and $a = 0.55f$.

for $\text{sgn}[\prod_{j=1}^2(\gamma_j + \chi(k_z)e^{i\theta})] = \pm 1$. Satisfied by discrete θ and k_z , it gives a nodal-point semimetal.

It is interesting to see that we not only can control the number and the position of the Dirac nodes but also can create nodal-line semimetal from the static nodal-point one by virtue of the periodic driving.

Second, we establish the BCC from $\mathcal{H}_{\text{eff}}(\mathbf{k})$ for our system. Although $\mathcal{H}_{\text{eff}}(\mathbf{k})$ inherits the inversion and mirror-rotation symmetries, it does not have the time-reversal and chiral symmetries [90]. To recover the symmetries, we make two unitary transformations $G_j(\mathbf{k}) = e^{i(-1)^j \mathcal{H}_j(\mathbf{k})T_j/2}$ and obtain $\tilde{\mathcal{H}}_{\text{eff},j}(\mathbf{k}) = G_j(\mathbf{k})\mathcal{H}_{\text{eff}}(\mathbf{k})G_j^{-1}(\mathbf{k})$ [76]. Respecting the time-reversal and chiral symmetries, $\tilde{\mathcal{H}}_{\text{eff},j}(\mathbf{k})$ have well-defined mirror-graded winding numbers \mathcal{W}_j . Since the transformations do not change the quasienergies, the SOTIs in $\mathcal{H}_{\text{eff}}(\mathbf{k})$ at

the quasienergies zero and π/T are described by \mathcal{W}_j as

$$\mathcal{W}_0 = (\mathcal{W}_1 + \mathcal{W}_2)/2, \quad \mathcal{W}_{\pi/T} = (\mathcal{W}_1 - \mathcal{W}_2)/2. \quad (7)$$

Reflecting the firm BCC, the numbers of the zero- and π/T -mode corner states equal to $4|\mathcal{W}_0|$ and $4|\mathcal{W}_{\pi/T}|$. The k_z -dependent SOTIs form a 3D SOTSMs, which hosts second-order Dirac nodes at the critical points of a 2D topological phase transition and hinge Fermi arcs from the distribution of the corner states. Note that it is equivalent to deem that $\mathcal{H}_{\text{eff}}(\mathbf{k})$ has hidden time-reversal and chiral symmetries under the redefined operations $G_j^{-1}(-\mathbf{k})\mathcal{T}G_j(\mathbf{k})$ and $G_j^{-1}(\mathbf{k})\mathcal{S}G_j(\mathbf{k})$ [90].

We demonstrate the constructive role of the periodic driving in generating novel Dirac nodal-point SOTSMs in Fig. 2. The quasienergy spectrum under the x -direction open boundary in Fig. 2(a) shows a topologically trivial phase, while the one under the x, y -direction open boundary in Fig. 2(b) shows rich topological phases in both the quasienergies zero and π/T . It signifies the diverse topological phases trivial in the first order but nontrivial in the second order. The Dirac nodal points in Fig. 2(b) at $k_z = 0.15\pi, 0.54\pi, 0.28\pi$, and 0.62π are well explained by Eq. (6) with $z_{\pi,-} = -2, -3, z_{0,-} = -1$ and 0 , respectively. Compared with the static case, the number of the nodal points is dramatically enhanced. It verifies the periodic driving as a useful way to manipulate the nodal points. The 2D SOTIs are completely characterized by the winding number \mathcal{W}_j defined in $\tilde{\mathcal{H}}_{\text{eff},j}$. The numbers $4|\mathcal{W}_0|$ and $4|\mathcal{W}_{\pi/T}|$ correctly count the zero- and π/T -mode corner states [see Fig. 2(c)]. Another interesting result is that the chiralities of the adjacent Dirac nodal points possess the same sign instead of the opposite sign in the static case. This explains why more corner states than the static case are created by the periodic driving. It also endows the Dirac nodal points in our periodic system with robustness to the perturbation-induced annihilation, which is only sensitive to the nodal points with opposite chiralities [55]. Both of the zero- and π/T -mode corner states contribute the hinge Fermi arcs [see Figs. 2(d) and 2(e)] of the SOTSMs.

To give a global picture of the Dirac nodal-point SOTSMs in our periodic system, we plot in Figs. 2(f) and 2(g) the phase diagram characterized by \mathcal{W}_0 and $\mathcal{W}_{\pi/T}$ in the k_z - T_2 plane. Much richer 2D-sliced SOTIs with a widely tunable number of zero- and π/T -mode corner states than the static case in Fig. 1(b) are created by the periodic driving. The phase boundaries well described by Eq. (6) correspond to the Dirac nodal points of the SOTSMs. Different from the static case, where the Dirac nodal points separate the trivial and SOTIs, the ones in our periodic system also separate the SOTIs with a different number of corner states. A clear tendency with the increase of the period T_2 is that the number of the Dirac nodal points increases, which can be analytically understood from Eq. (6).

Next, we create the Dirac nodal-loop SOTSMs from the static nodal-point ones via engineering the periodic driving to satisfy Eqs. (5). The quasienergy spectrum in

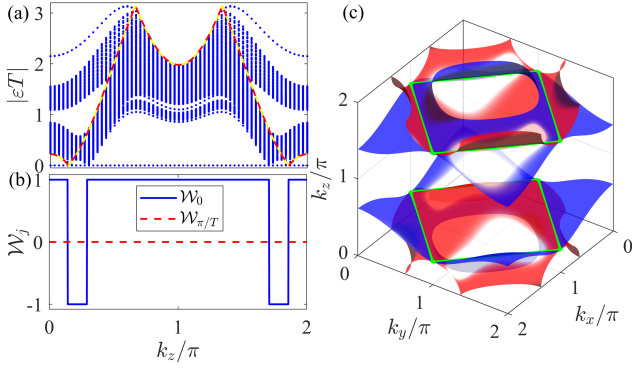


FIG. 3. (a) Quasienergy spectrum under the x, y -direction open boundary condition. The dispersion relations of $\theta = \pi$ (yellow solid line) and 0 (red dashed line) determine the Dirac nodal points. (b) Mirror-graded winding numbers for the zero- and π/T -mode corner states. (c) Surfaces in BZ satisfying Eqs. (5) with $z_j = 1$ for $j = 1$ (red) and 2 (blue). The green solid line is the intersecting line of the two surfaces. We use $T_1 = T_2 = f^{-1}$, $q_2 = -q_1 = 1$, $\lambda = 1.5f$, and $a = 0.8f$.

Fig. 3(a) reveals that, besides the zero-mode Dirac nodal points at $k_z = 0.14\pi$ and 1.86π , recoverable by Eq. (6) with $z_{\pi/0,+} = 2$, and the π/T -mode ones at $k_z = 0.66\pi$ and 1.34π , recoverable by Eq. (6) with $z_{\pi/0,+} = 1$, there are two extra band-touching points at $k_z = 0.29\pi$ and 1.71π . Plotting the two surfaces governed by Eqs. (5) in the BZ in Fig. 3(c), we really see two closed intersecting lines at $k_z = 0.29\pi$ and 1.71π . It confirms the presence of two parallel nodal loops. The associated mirror-graded winding numbers in Fig. 3(b) show that both of the nodal points and loops cause the second-order topological phase transition, which endows them with the second-order feature. All these results verify the formation of a novel SOTSM with coexisting nodal points and loops via periodically driving a static Dirac nodal-point one. Such phase has not been found in static systems. Although a similar semimetal with coexisting nodal points and loops was reported in the static system [94], it is in the first-order Weyl type. However, ours is in the second-order Dirac type and protected by both \mathcal{P} and \mathcal{T} symmetries. The result proves the distinguished role of the periodic driving in creating exotic matters absent in static systems.

B. Weyl SOTSMs via Floquet engineering

Our periodic driving scheme (2) can be used to create novel Weyl SOTSMs by introducing a perturbation $\Delta\mathcal{H} = ip\Gamma_1\Gamma_3$ to break the \mathcal{T} symmetry. The quasienergy spectrum in Fig. 4(a) reveals that each Dirac point in Fig. 2(a) splits into two Weyl points with a Chern insulator formed between them. Each Weyl point can be analytically explained by our band-touching condition [90]. The Chern insulator is signified by the gapless chiral boundary states, which can be topologically wit-

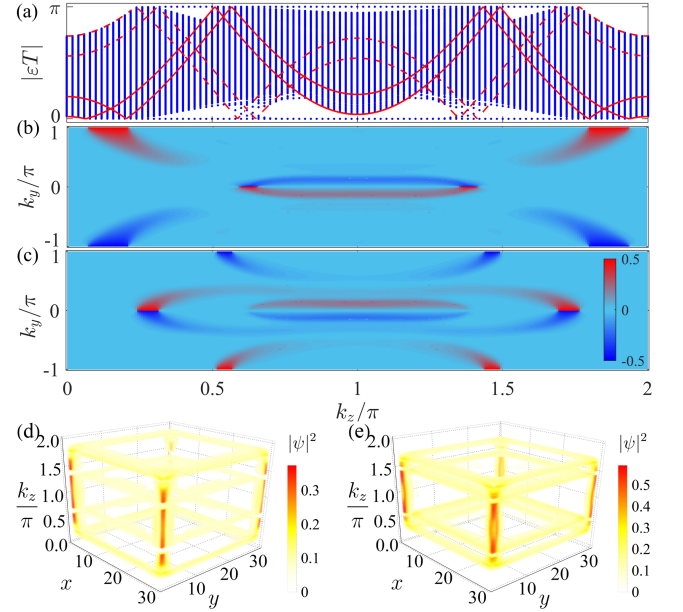


FIG. 4. (a) Quasienergy spectra under the x, y -direction open boundary condition. Wannier centers for the zero (b) and π/T (c) quasienergy gaps. Coexisting surface and hinge Fermi arcs contributed by the zero-(d) and π/T -mode (e) first-order boundary and second-order corner states. We use $p = 0.07f$ and the others being same as Fig. 2.

nessed by the Wannier center [65]. The Wannier center of the zero- and π/T -mode gaps jumping from -0.5 to 0.5 when k_y runs from $-\pi$ to π verifies the formation of a Chern band [see Figs. 4(b) and 4(c)], which contributes the surface Fermi arcs. Therefore, we have realized a hybrid-order Weyl semimetal, which is featured with the coexisting first- and second-order Weyl points as well as the surface and hinge Fermi arcs [see Figs. 4(d) and 4(e)]. This result dramatically enriches the family of the recently proposed purely second-order Weyl semimetal in static systems [65, 66]. Another novel character of our periodic system is that it possesses a rich hybrid of topological phases in the zero and π/T modes for a given k_z in the 2D-sliced subsystem, which can be any combination of normal insulator, Chern insulator, and SOTI in the zero and π/T modes. This is also absent in static systems. All of these results confirm again the superiority of the periodic driving in freely tuning and synthesizing exotic topological matters. Note that the hybrid-order nature of the Weyl semimetal in our periodic system does not depend on the form of the \mathcal{T} -symmetry breaking perturbation. To other forms, the explicit locations on forming the Weyl points may be different, but the conclusion that a Chern band is present between each pair of Weyl points does not change.

IV. DISCUSSION AND CONCLUSION

Although we only show the generation of the same order of semimetals as the static case, the periodic driving also has the ability to create the SOTSMs from the static first-order semimetal or even normal insulator [90]. The step like driving protocol is considered just for analytical solvability. Our scheme is generalizable to other driving forms. The SOTSMs have been predicted in Cd_3As_2 , KMgBi , and PtO_2 [61, 95] and realized in classical acoustic metamaterials [67, 68]. Periodic driving has exhibited its power in engineering exotic phases in electronic material [74, 96], ultracold atoms [97], superconductor qubits [73], and photonics [71, 72, 98, 99]. The progress indicates that our result is realizable in the recent experimental state of the art.

In summary, we have investigated the exotic SOTSMs induced by periodic driving. It is revealed that the pe-

riodic driving provides a sufficient freedom in creating novel SOTSMs absent in static systems. The discovered widely tunable number of nodes and hinge Fermi arcs, the adjacent nodes with same chirality, and the coexisting nodal points and nodal loops in Dirac SOTSMs and the hybrid-order Weyl semimetals with the coexisting hinge and surface Fermi arcs dramatically enrich the family of topological semimetals in natural materials. Our result indicates that the periodic driving supplies a feasible and convenient way to explore the exotic semimetal physics by adding the time periodicity as a novel control dimension. This significantly reduces the difficulties in fabricating specific material structure in static systems.

ACKNOWLEDGMENTS

The work is supported by the National Natural Science Foundation (Grants No. 11875150, No. 11834005, and No. 12047501).

-
- [1] M. Z. Hasan and C. L. Kane, Colloquium: Topological insulators, *Rev. Mod. Phys.* **82**, 3045 (2010).
 - [2] X.-L. Qi and S.-C. Zhang, Topological insulators and superconductors, *Rev. Mod. Phys.* **83**, 1057 (2011).
 - [3] C.-K. Chiu, J. C. Y. Teo, A. P. Schnyder, and S. Ryu, Classification of topological quantum matter with symmetries, *Rev. Mod. Phys.* **88**, 035005 (2016).
 - [4] N. P. Armitage, E. J. Mele, and A. Vishwanath, Weyl and Dirac semimetals in three-dimensional solids, *Rev. Mod. Phys.* **90**, 015001 (2018).
 - [5] B. Q. Lv, T. Qian, and H. Ding, Experimental perspective on three-dimensional topological semimetals, *Rev. Mod. Phys.* **93**, 025002 (2021).
 - [6] W. A. Benalcazar, B. A. Bernevig, and T. L. Hughes, Quantized electric multipole insulators, *Science* **357**, 61 (2017).
 - [7] J. Langbehn, Y. Peng, L. Trifunovic, F. von Oppen, and P. W. Brouwer, Reflection-symmetric second-order topological insulators and superconductors, *Phys. Rev. Lett.* **119**, 246401 (2017).
 - [8] Z. Song, Z. Fang, and C. Fang, $(d-2)$ -dimensional edge states of rotation symmetry protected topological states, *Phys. Rev. Lett.* **119**, 246402 (2017).
 - [9] F. Schindler, A. M. Cook, M. G. Vergniory, Z. Wang, S. S. P. Parkin, B. A. Bernevig, and T. Neupert, Higher-order topological insulators, *Science Advances* **4**, eaat0346 (2018).
 - [10] Z. Yan, F. Song, and Z. Wang, Majorana corner modes in a high-temperature platform, *Phys. Rev. Lett.* **121**, 096803 (2018).
 - [11] M. Ezawa, Topological switch between second-order topological insulators and topological crystalline insulators, *Phys. Rev. Lett.* **121**, 116801 (2018).
 - [12] F. Liu, H.-Y. Deng, and K. Wakabayashi, Helical topological edge states in a quadrupole phase, *Phys. Rev. Lett.* **122**, 086804 (2019).
 - [13] R.-X. Zhang, W. S. Cole, X. Wu, and S. Das Sarma, Higher-order topology and nodal topological superconductivity in $\text{Fe}(\text{Se},\text{Te})$ heterostructures, *Phys. Rev. Lett.* **123**, 167001 (2019).
 - [14] M. J. Park, Y. Kim, G. Y. Cho, and S. Lee, Higher-order topological insulator in twisted bilayer graphene, *Phys. Rev. Lett.* **123**, 216803 (2019).
 - [15] X.-L. Sheng, C. Chen, H. Liu, Z. Chen, Z.-M. Yu, Y. X. Zhao, and S. A. Yang, Two-dimensional second-order topological insulator in graphdiyne, *Phys. Rev. Lett.* **123**, 256402 (2019).
 - [16] A. Tiwari, M.-H. Li, B. A. Bernevig, T. Neupert, and S. A. Parameswaran, Unhinging the surfaces of higher-order topological insulators and superconductors, *Phys. Rev. Lett.* **124**, 046801 (2020).
 - [17] Y. Ren, Z. Qiao, and Q. Niu, Engineering corner states from two-dimensional topological insulators, *Phys. Rev. Lett.* **124**, 166804 (2020).
 - [18] Q.-B. Zeng, Y.-B. Yang, and Y. Xu, Higher-order topological insulators and semimetals in generalized Aubry-André-Harper models, *Phys. Rev. B* **101**, 241104(R) (2020).
 - [19] R.-J. Slager, L. Rademaker, J. Zaanen, and L. Balents, Impurity-bound states and Green's function zeros as local signatures of topology, *Phys. Rev. B* **92**, 085126 (2015).
 - [20] W. Zhang, X. Xie, H. Hao, J. Dang, S. Xiao, S. Shi, H. Ni, Z. Niu, C. Wang, K. Jin, X. Zhang, and X. Xu, Low-threshold topological nanolasers based on the second-order corner state, *Light. Sci. Appl.* **9**, 109 (2020).
 - [21] M. Serra-Garcia, V. Peri, R. Süsstrunk, O. R. Bilal, T. Larsen, L. G. Villanueva, and S. D. Huber, Observation of a phononic quadrupole topological insulator, *Nature* **555**, 342 (2018).
 - [22] C. W. Peterson, W. A. Benalcazar, T. L. Hughes, and G. Bahl, A quantized microwave quadrupole insulator with topologically protected corner states, *Nature* **555**, 346 (2018).
 - [23] F. Schindler, Z. Wang, M. G. Vergniory, A. M. Cook, A. Murani, S. Sengupta, A. Y. Kasumov, R. Deblock, S. Jeon, I. Drozdov, H. Bouchiat, S. Guéron, A. Yazdani,

- B. A. Bernevig, and T. Neupert, Higher-order topology in bismuth, *Nature Physics* **14**, 918 (2018).
- [24] S. Imhof, C. Berger, F. Bayer, J. Brehm, L. W. Molenkamp, T. Kiessling, F. Schindler, C. H. Lee, M. Greiter, T. Neupert, and R. Thomale, Topoelectrical-circuit realization of topological corner modes, *Nature Physics* **14**, 925 (2018).
- [25] J. Wu, X. Huang, J. Lu, Y. Wu, W. Deng, F. Li, and Z. Liu, Observation of corner states in second-order topological electric circuits, *Phys. Rev. B* **102**, 104109 (2020).
- [26] H. Fan, B. Xia, L. Tong, S. Zheng, and D. Yu, Elastic higher-order topological insulator with topologically protected corner states, *Phys. Rev. Lett.* **122**, 204301 (2019).
- [27] X.-D. Chen, W.-M. Deng, F.-L. Shi, F.-L. Zhao, M. Chen, and J.-W. Dong, Direct observation of corner states in second-order topological photonic crystal slabs, *Phys. Rev. Lett.* **122**, 233902 (2019).
- [28] B.-Y. Xie, G.-X. Su, H.-F. Wang, H. Su, X.-P. Shen, P. Zhan, M.-H. Lu, Z.-L. Wang, and Y.-F. Chen, Visualization of higher-order topological insulating phases in two-dimensional dielectric photonic crystals, *Phys. Rev. Lett.* **122**, 233903 (2019).
- [29] Z.-Z. Yang, X. Li, Y.-Y. Peng, X.-Y. Zou, and J.-C. Cheng, Helical higher-order topological states in an acoustic crystalline insulator, *Phys. Rev. Lett.* **125**, 255502 (2020).
- [30] Y. Yang, J. Lu, M. Yan, X. Huang, W. Deng, and Z. Liu, Hybrid-order topological insulators in a phononic crystal, *Phys. Rev. Lett.* **126**, 156801 (2021).
- [31] Z. K. Liu, B. Zhou, Y. Zhang, Z. J. Wang, H. M. Weng, D. Prabhakaran, S.-K. Mo, Z. X. Shen, Z. Fang, X. Dai, Z. Hussain, and Y. L. Chen, Discovery of a three-dimensional topological Dirac semimetal, Na_3Bi , *Science* **343**, 864 (2014).
- [32] M. Neupane, S.-Y. Xu, R. Sankar, N. Alidoust, G. Bian, C. Liu, I. Belopolski, T.-R. Chang, H.-T. Jeng, H. Lin, A. Bansil, F. Chou, and M. Z. Hasan, Observation of a three-dimensional topological Dirac semimetal phase in high-mobility Cd_3As_2 , *Nature Communications* **5**, 3786 (2014).
- [33] S. Borisenko, Q. Gibson, D. Evtushinsky, V. Zabolotnyy, B. Büchner, and R. J. Cava, Experimental realization of a three-dimensional Dirac semimetal, *Phys. Rev. Lett.* **113**, 027603 (2014).
- [34] S.-Y. Xu, C. Liu, S. K. Kushwaha, R. Sankar, J. W. Krizan, I. Belopolski, M. Neupane, G. Bian, N. Alidoust, T.-R. Chang, H.-T. Jeng, C.-Y. Huang, W.-F. Tsai, H. Lin, P. P. Shibaev, F.-C. Chou, R. J. Cava, and M. Z. Hasan, Observation of Fermi arc surface states in a topological metal, *Science* **347**, 294 (2015).
- [35] S. M. Young, S. Zaheer, J. C. Y. Teo, C. L. Kane, E. J. Mele, and A. M. Rappe, Dirac semimetal in three dimensions, *Phys. Rev. Lett.* **108**, 140405 (2012).
- [36] Z. Wang, Y. Sun, X.-Q. Chen, C. Franchini, G. Xu, H. Weng, X. Dai, and Z. Fang, Dirac semimetal and topological phase transitions in A_3Bi ($\text{A} = \text{Na}, \text{K}, \text{Rb}$), *Phys. Rev. B* **85**, 195320 (2012).
- [37] Z. Wang, H. Weng, Q. Wu, X. Dai, and Z. Fang, Three-dimensional Dirac semimetal and quantum transport in Cd_3As_2 , *Phys. Rev. B* **88**, 125427 (2013).
- [38] R. Y. Chen, Z. G. Chen, X.-Y. Song, J. A. Schneeloch, G. D. Gu, F. Wang, and N. L. Wang, Magnetoinfrared spectroscopy of Landau levels and Zeeman splitting of three-dimensional massless Dirac Fermions in ZrTe_5 , *Phys. Rev. Lett.* **115**, 176404 (2015).
- [39] Y. Liu, X. Yuan, C. Zhang, Z. Jin, A. Narayan, C. Luo, Z. Chen, L. Yang, J. Zou, X. Wu, S. Sanvito, Z. Xia, L. Li, Z. Wang, and F. Xiu, Zeeman splitting and dynamical mass generation in Dirac semimetal ZrTe_5 , *Nature Communications* **7**, 12516 (2016).
- [40] X. Wan, A. M. Turner, A. Vishwanath, and S. Y. Savrasov, Topological semimetal and Fermi-arc surface states in the electronic structure of pyrochlore iridates, *Phys. Rev. B* **83**, 205101 (2011).
- [41] A. A. Burkov and L. Balents, Weyl semimetal in a topological insulator multilayer, *Phys. Rev. Lett.* **107**, 127205 (2011).
- [42] H. Weng, C. Fang, Z. Fang, B. A. Bernevig, and X. Dai, Weyl semimetal phase in noncentrosymmetric transition-metal monophosphides, *Phys. Rev. X* **5**, 011029 (2015).
- [43] S.-M. Huang, S.-Y. Xu, I. Belopolski, C.-C. Lee, G. Chang, B. Wang, N. Alidoust, G. Bian, M. Neupane, C. Zhang, S. Jia, A. Bansil, H. Lin, and M. Z. Hasan, A Weyl Fermion semimetal with surface Fermi arcs in the transition metal mononitride TaAs class, *Nature Communications* **6**, 7373 (2015).
- [44] S.-Y. Xu, I. Belopolski, N. Alidoust, M. Neupane, G. Bian, C. Zhang, R. Sankar, G. Chang, Z. Yuan, C.-C. Lee, S.-M. Huang, H. Zheng, J. Ma, D. S. Sanchez, B. Wang, A. Bansil, F. Chou, P. P. Shibaev, H. Lin, S. Jia, and M. Z. Hasan, Discovery of a Weyl Fermion semimetal and topological Fermi arcs, *Science* **349**, 613 (2015).
- [45] B. Q. Lv, H. M. Weng, B. B. Fu, X. P. Wang, H. Miao, J. Ma, P. Richard, X. C. Huang, L. X. Zhao, G. F. Chen, Z. Fang, X. Dai, T. Qian, and H. Ding, Experimental discovery of Weyl semimetal TaAs , *Phys. Rev. X* **5**, 031013 (2015).
- [46] L. X. Yang, Z. K. Liu, Y. Sun, H. Peng, H. F. Yang, T. Zhang, B. Zhou, Y. Zhang, Y. F. Guo, M. Rahn, D. Prabhakaran, Z. Hussain, S.-K. Mo, C. Felser, B. Yan, and Y. L. Chen, Weyl semimetal phase in the noncentrosymmetric compound TaAs , *Nature Physics* **11**, 728 (2015).
- [47] X. Huang, L. Zhao, Y. Long, P. Wang, D. Chen, Z. Yang, H. Liang, M. Xue, H. Weng, Z. Fang, X. Dai, and G. Chen, Observation of the chiral-anomaly-induced negative magnetoresistance in 3d Weyl semimetal TaAs , *Phys. Rev. X* **5**, 031023 (2015).
- [48] S.-Y. Xu, N. Alidoust, I. Belopolski, Z. Yuan, G. Bian, T.-R. Chang, H. Zheng, V. N. Strocov, D. S. Sanchez, G. Chang, C. Zhang, D. Mou, Y. Wu, L. Huang, C.-C. Lee, S.-M. Huang, B. Wang, A. Bansil, H.-T. Jeng, T. Neupert, A. Kaminski, H. Lin, S. Jia, and M. Zahid Hasan, Discovery of a Weyl Fermion state with Fermi arcs in niobium arsenide, *Nature Physics* **11**, 748 (2015).
- [49] C. Shekhar, A. K. Nayak, Y. Sun, M. Schmidt, M. Nicklas, I. Leermakers, U. Zeitler, Y. Skourski, J. Wosnitza, Z. Liu, Y. Chen, W. Schnelle, H. Borrmann, Y. Grin, C. Felser, and B. Yan, Extremely large magnetoresistance and ultrahigh mobility in the topological Weyl semimetal candidate NbP , *Nature Physics* **11**, 645 (2015).
- [50] L. Lu, L. Fu, J. D. Joannopoulos, and M. Soljačić, Weyl points and line nodes in gyroid photonic crystals, *Nature Photonics* **7**, 294 (2013).
- [51] L. Lu, Z. Wang, D. Ye, L. Ran, L. Fu, J. D. Joannopoulos, and M. Soljačić, Experimental observation of Weyl points, *Science* **349**, 622 (2015).

- [52] A. A. Soluyanov, D. Gresch, Z. Wang, Q. Wu, M. Troyer, X. Dai, and B. A. Bernevig, Type-II Weyl semimetals, *Nature* **527**, 495 (2015).
- [53] Y. Xu, F. Zhang, and C. Zhang, Structured Weyl points in spin-orbit coupled fermionic superfluids, *Phys. Rev. Lett.* **115**, 265304 (2015).
- [54] T. Nguyen, F. Han, N. Andrejevic, R. Pablo-Pedro, A. Apte, Y. Tsurimaki, Z. Ding, K. Zhang, A. Alatas, E. E. Alp, S. Chi, J. Fernandez-Baca, M. Matsuda, D. A. Tennant, Y. Zhao, Z. Xu, J. W. Lynn, S. Huang, and M. Li, Topological singularity induced chiral Kohn anomaly in a Weyl semimetal, *Phys. Rev. Lett.* **124**, 236401 (2020).
- [55] A. A. Burkov, M. D. Hook, and L. Balents, Topological nodal semimetals, *Phys. Rev. B* **84**, 235126 (2011).
- [56] Z. Yan, R. Bi, H. Shen, L. Lu, S.-C. Zhang, and Z. Wang, Nodal-link semimetals, *Phys. Rev. B* **96**, 041103(R) (2017).
- [57] R. Bi, Z. Yan, L. Lu, and Z. Wang, Nodal-knot semimetals, *Phys. Rev. B* **96**, 201305(R) (2017).
- [58] A. Samanta, D. P. Arovas, and A. Auerbach, Hall coefficient of semimetals, *Phys. Rev. Lett.* **126**, 076603 (2021).
- [59] S. Sengupta, M. N. Y. Lhachemi, and I. Garate, Phonon magnetochiral effect of band-geometric origin in Weyl semimetals, *Phys. Rev. Lett.* **125**, 146402 (2020).
- [60] M. Lin and T. L. Hughes, Topological quadrupolar semimetals, *Phys. Rev. B* **98**, 241103(R) (2018).
- [61] B. J. Wieder, Z. Wang, J. Cano, X. Dai, L. M. Schoop, B. Bradlyn, and B. A. Bernevig, Strong and fragile topological dirac semimetals with higher-order fermi arcs, *Nature Communications* **11**, 627 (2020).
- [62] W. Wu, Z.-M. Yu, X. Zhou, Y. X. Zhao, and S. A. Yang, Higher-order Dirac Fermions in three dimensions, *Phys. Rev. B* **101**, 205134 (2020).
- [63] B. Roy, Higher-order topological superconductors in \mathcal{P} -, \mathcal{T} -odd quadrupolar Dirac materials, *Phys. Rev. B* **101**, 220506(R) (2020).
- [64] K. Wang, J.-X. Dai, L. B. Shao, S. A. Yang, and Y. X. Zhao, Boundary criticality of \mathcal{PT} -invariant topology and second-order nodal-line semimetals, *Phys. Rev. Lett.* **125**, 126403 (2020).
- [65] H.-X. Wang, Z.-K. Lin, B. Jiang, G.-Y. Guo, and J.-H. Jiang, Higher-order Weyl semimetals, *Phys. Rev. Lett.* **125**, 146401 (2020).
- [66] S. A. A. Ghorashi, T. Li, and T. L. Hughes, Higher-order Weyl semimetals, *Phys. Rev. Lett.* **125**, 266804 (2020).
- [67] L. Luo, H.-X. Wang, Z.-K. Lin, B. Jiang, Y. Wu, F. Li, and J.-H. Jiang, Observation of a phononic higher-order Weyl semimetal, *Nature Materials* **20**, 794 (2021).
- [68] Q. Wei, X. Zhang, W. Deng, J. Lu, X. Huang, M. Yan, G. Chen, Z. Liu, and S. Jia, Higher-order topological semimetal in acoustic crystals, *Nature Materials* **20**, 812 (2021).
- [69] A. Eckardt, Colloquium: Atomic quantum gases in periodically driven optical lattices, *Rev. Mod. Phys.* **89**, 011004 (2017).
- [70] F. Meinert, M. J. Mark, K. Lauber, A. J. Daley, and H.-C. Nägerl, Floquet engineering of correlated tunneling in the Bose-Hubbard model with ultracold atoms, *Phys. Rev. Lett.* **116**, 205301 (2016).
- [71] M. C. Rechtsman, J. M. Zeuner, Y. Plotnik, Y. Lumer, D. Podolsky, F. Dreisow, S. Nolte, M. Segev, and A. Szameit, Photonic Floquet topological insulators, *Nature (London)* **496**, 196 (2013).
- [72] Q. Cheng, Y. Pan, H. Wang, C. Zhang, D. Yu, A. Gover, H. Zhang, T. Li, L. Zhou, and S. Zhu, Observation of anomalous π modes in photonic Floquet engineering, *Phys. Rev. Lett.* **122**, 173901 (2019).
- [73] P. Roushan, C. Neill, A. Megrant, Y. Chen, R. Babush, R. Barends, B. Campbell, Z. Chen, B. Chiaro, A. Dunsworth, A. Fowler, E. Jeffrey, J. Kelly, E. Lucero, J. Mutus, P. J. J. O'Huallachain, M. Neeley, C. Quintana, D. Sank, A. Vainsencher, J. Wenner, T. White, E. Kapit, H. Neven, and J. Martinis, Chiral ground-state currents of interacting photons in a synthetic magnetic field, *Nature Physics* **13**, 146 (2017).
- [74] J. W. McIver, B. Schulte, F.-U. Stein, T. Matsuyama, G. Jotzu, G. Meier, and A. Cavalleri, Light-induced anomalous Hall effect in graphene, *Nature Physics* **16**, 38 (2020).
- [75] T.-S. Xiong, J. Gong, and J.-H. An, Towards large-Chern-number topological phases by periodic quenching, *Phys. Rev. B* **93**, 184306 (2016).
- [76] H. Liu, T.-S. Xiong, W. Zhang, and J.-H. An, Floquet engineering of exotic topological phases in systems of cold atoms, *Phys. Rev. A* **100**, 023622 (2019).
- [77] L. Li, C. H. Lee, and J. Gong, Realistic Floquet semimetal with exotic topological linkages between arbitrarily many nodal loops, *Phys. Rev. Lett.* **121**, 036401 (2018).
- [78] H. Wu and J.-H. An, Floquet topological phases of non-Hermitian systems, *Phys. Rev. B* **102**, 041119(R) (2020).
- [79] A. Kundu, H. A. Fertig, and B. Seradjeh, Effective theory of Floquet topological transitions, *Phys. Rev. Lett.* **113**, 236803 (2014).
- [80] H. Wu, B.-Q. Wang, and J.-H. An, Floquet second-order topological insulators in non-Hermitian systems, *Phys. Rev. B* **103**, L041115 (2021).
- [81] Y. Peng and G. Refael, Floquet second-order topological insulators from nonsymmorphic space-time symmetries, *Phys. Rev. Lett.* **123**, 016806 (2019).
- [82] R. W. Bomantara, L. Zhou, J. Pan, and J. Gong, Coupled-wire construction of static and Floquet second-order topological insulators, *Phys. Rev. B* **99**, 045441 (2019).
- [83] R. Seshadri, A. Dutta, and D. Sen, Generating a second-order topological insulator with multiple corner states by periodic driving, *Phys. Rev. B* **100**, 115403 (2019).
- [84] H. Hu, B. Huang, E. Zhao, and W. V. Liu, Dynamical singularities of Floquet higher-order topological insulators, *Phys. Rev. Lett.* **124**, 057001 (2020).
- [85] B. Huang and W. V. Liu, Floquet higher-order topological insulators with anomalous dynamical polarization, *Phys. Rev. Lett.* **124**, 216601 (2020).
- [86] A. K. Ghosh, T. Nag, and A. Saha, Floquet generation of a second-order topological superconductor, *Phys. Rev. B* **103**, 045424 (2021).
- [87] T. Nag, V. Jurić, and B. Roy, Hierarchy of higher-order Floquet topological phases in three dimensions, *Phys. Rev. B* **103**, 115308 (2021).
- [88] M. Rodriguez-Vega, A. Kumar, and B. Seradjeh, Higher-order Floquet topological phases with corner and bulk bound states, *Phys. Rev. B* **100**, 085138 (2019).
- [89] W. B. Rui, S.-B. Zhang, M. M. Hirschmann, Z. Zheng, A. P. Schnyder, B. Trauzettel, and Z. D. Wang, Higher-order Weyl superconductors with anisotropic Weyl-point connectivity, *Phys. Rev. B* **103**, 184510 (2021).

- [90] See the Supplemental Material for the real-space Hamiltonian, the definitions of the mirror-graded winding number and the chirality, the symmetry analysis, the derivation of the condition to form the Dirac/Weyl nodes, and the definition of Wilson loop.
- [91] W. A. Benalcazar, B. A. Bernevig, and T. L. Hughes, Electric multipole moments, topological multipole moment pumping, and chiral hinge states in crystalline insulators, *Phys. Rev. B* **96**, 245115 (2017).
- [92] H. Sambe, Steady states and quasienergies of a quantum-mechanical system in an oscillating field, *Phys. Rev. A* **7**, 2203 (1973).
- [93] C. Chen, J.-H. An, H.-G. Luo, C. P. Sun, and C. H. Oh, Floquet control of quantum dissipation in spin chains, *Phys. Rev. A* **91**, 052122 (2015).
- [94] Y.-H. Lu, B.-Z. Wang, and X.-J. Liu, Ideal Weyl semimetal with 3d spin-orbit coupled ultracold quantum gas, *Science Bulletin* **65**, 2080 (2020).
- [95] C.-Z. Li, A.-Q. Wang, C. Li, W.-Z. Zheng, A. Brinkman, D.-P. Yu, and Z.-M. Liao, Reducing electronic transport dimension to topological hinge states by increasing geometry size of dirac semimetal josephson junctions, *Phys. Rev. Lett.* **124**, 156601 (2020).
- [96] F. Mahmood, C.-K. Chan, Z. Alpichshev, D. Gardner, Y. Lee, P. A. Lee, and N. Gedik, Selective scattering between floquet-bloch and volkov states in a topological insulator, *Nat. Phys.* **12**, 306 (2016).
- [97] K. Wintersperger, C. Braun, F. N. Ünal, A. Eckardt, M. D. Liberto, N. Goldman, I. Bloch, and M. Aidelsburger, Realization of an anomalous floquet topological system with ultracold atoms, *Nat. Phys.* **16**, 1058 (2020).
- [98] S. Mukherjee, A. Spracklen, M. Valiente, E. Andersson, P. Öhberg, N. Goldman, and R. R. Thomson, Experimental observation of anomalous topological edge modes in a slowly driven photonic lattice, *Nature Communications* **8**, 13918 (2017).
- [99] L. J. Maczewsky, J. M. Zeuner, S. Nolte, and A. Szameit, Observation of photonic anomalous floquet topological insulators, *Nat. Commun.* **8**, 13756 (2017).

Supplemental material for “Engineering exotic second-order topological semimetals by periodic driving”

Bao-Qin Wang,^{1,*} Hong Wu,^{1,*} and Jun-Hong An^{1,†}

¹Lanzhou Center for Theoretical Physics, Key Laboratory of Theoretical Physics of Gansu Province, Lanzhou University, Lanzhou 730000, China

CONTENTS

S1. Real-space Hamiltonian and mirror-graded winding number	1
S2. Chirality of Dirac points	1
S3. Floquet Hamiltonian	2
S4. Symmetry analysis	3
S5. Weyl nodes	3
S6. Wilson loop	4
S7. Conversion of different orders of semimetals	4
References	5

S1. REAL-SPACE HAMILTONIAN AND MIRROR-GRADED WINDING NUMBER

We investigate a system of spinless fermions moving on a 3D lattice. Its real-space Hamiltonian reads

$$\begin{aligned} \hat{H} = \sum_{\mathbf{r}} \{ & \gamma [\hat{c}_{\mathbf{r},1}^\dagger (\hat{c}_{\mathbf{r},3} + \hat{c}_{\mathbf{r},4}) + \hat{c}_{\mathbf{r},2}^\dagger (\hat{c}_{\mathbf{r},4} - \hat{c}_{\mathbf{r},3})] \\ & + \lambda [\hat{c}_{\mathbf{r},1}^\dagger (\hat{c}_{\mathbf{r}+x,3} + \hat{c}_{\mathbf{r}+y,4}) + \hat{c}_{\mathbf{r},2}^\dagger (\hat{c}_{\mathbf{r}-x,4} - \hat{c}_{\mathbf{r}-y,3})] \\ & + \frac{a}{2} [\hat{c}_{\mathbf{r},1}^\dagger (\hat{c}_{\mathbf{r}+x+z,3} + \hat{c}_{\mathbf{r}+y+z,4}) + \hat{c}_{\mathbf{r},2}^\dagger (\hat{c}_{\mathbf{r}-x+z,4} \\ & - \hat{c}_{\mathbf{r}-y+z,3}) + \hat{c}_{\mathbf{r},3}^\dagger (\hat{c}_{\mathbf{r}-x+z,1} - \hat{c}_{\mathbf{r}+y+z,2}) \\ & + \hat{c}_{\mathbf{r},4}^\dagger (\hat{c}_{\mathbf{r}+x+z,2} + \hat{c}_{\mathbf{r}-y+z,1})] + \text{H.c.} \}, \end{aligned} \quad (\text{S1})$$

where $\hat{c}_{\mathbf{r},i}$ ($i = 1, 2, 3, 4$) is the annihilation operator of the fermion at sublattice i of unit-cell site $\mathbf{r} = (x, y, z)$, λ , γ , and a are the intercell, intracell, and interlayer hopping rates, respectively. Our system is a 3D generalization of the Benalcazar-Bernevig-Hughes (BBH) model [1, 2], which is a 2D second-order topological insulators (SOTIs), by further considering the coupling between different layers. The 3D second-order topological semimetal (SOTSM) can be sliced into the stacking of 2D SOTIs and normal insulators.

The momentum-space Hamiltonian under the periodic boundary condition along all the three directions reads $\hat{H} = \sum_{\mathbf{k}} \hat{\mathbf{C}}_{\mathbf{k}}^\dagger \mathcal{H}(\mathbf{k}) \hat{\mathbf{C}}_{\mathbf{k}}$ with $\hat{\mathbf{C}}_{\mathbf{k}} = (\hat{c}_{\mathbf{k},1}^\dagger \hat{c}_{\mathbf{k},2}^\dagger \hat{c}_{\mathbf{k},3}^\dagger \hat{c}_{\mathbf{k},4}^\dagger)$ and

$$\begin{aligned} \mathcal{H}(\mathbf{k}) = & [\gamma + \chi(k_z) \cos k_x] \Gamma_5 - \chi(k_z) \sin k_x \Gamma_3 \\ & - [\gamma + \chi(k_z) \cos k_y] \Gamma_2 - \chi(k_z) \sin k_y \Gamma_1, \end{aligned} \quad (\text{S2})$$

where $\chi(k_z) = \lambda + a \cos k_z$, $\Gamma_1 = \tau_y \sigma_x$, $\Gamma_2 = \tau_y \sigma_y$, $\Gamma_3 = \tau_y \sigma_z$, $\Gamma_4 = \tau_z \sigma_0$, and $\Gamma_5 = \tau_x \sigma_0$, with τ_i and σ_i being Pauli matrices, τ_0 and σ_0 being identity matrices.

The second-order topology of the system with mirror-rotation and chiral symmetries can be described by the mirror-graded winding number [3]. The mirror-graded winding number is defined in the Hamiltonian $\mathcal{H}(\theta, \theta, k_z)$ along the high-symmetry line $k_x = k_y \equiv \theta$. After diagonalizing $\mathcal{H}(\theta, \theta, k_z)$ into $\text{diag}[\mathcal{H}^+(\theta, k_z), \mathcal{H}^-(\theta, k_z)]$ with $\mathcal{H}^\pm(\theta, k_z) = \mathbf{h}^\pm \cdot \boldsymbol{\sigma}$ and $\mathbf{h}^\pm = \sqrt{2}[\gamma + \chi(k_z) \cos \theta, \pm \chi(k_z) \sin \theta, 0]$, we define the mirror-graded winding number as

$$\mathcal{W}(k_z) = (\mathcal{W}_+ - \mathcal{W}_-)/2. \quad (\text{S3})$$

Here \mathcal{W}_\pm are the winding number associated with $\mathcal{H}^\pm(\theta, k_z)$ as

$$\begin{aligned} \mathcal{W}_\pm = & \frac{i}{2\pi} \int_0^{2\pi} \langle u_\pm(\theta, k_z) | \partial_\theta | u_\pm(\theta, k_z) \rangle d\theta \\ = & \frac{1}{2\pi} \int_0^{2\pi} (\mathbf{h}^\pm \times \partial_\theta \mathbf{h}^\pm) d\theta, \end{aligned} \quad (\text{S4})$$

where $\mathbf{h}^\pm = \mathbf{h}^\pm / |\mathbf{h}^\pm|$ and $|u_\pm(\theta, k_z)\rangle$ are the eigenstates of $\mathcal{H}^\pm(\theta, k_z)$.

S2. CHIRALITY OF DIRAC POINTS

Each Dirac node has a well-defined chirality. The chirality for the first-order node has been defined in Ref. [4]. We here give a definition of the chirality for a second-order one. Choosing a closed path c encircling the Dirac node $(k_0, k_0, k_{z,0})$, we define its chirality as

$$\mathcal{Q} = \frac{-i}{4\pi} \oint_c [\langle u_+(\mathbf{k}) | \nabla_{\mathbf{k}} | u_+(\mathbf{k}) \rangle - \langle u_-(\mathbf{k}) | \nabla_{\mathbf{k}} | u_-(\mathbf{k}) \rangle] \cdot d\mathbf{k}, \quad (\text{S5})$$

where $|u_\pm(\mathbf{k})\rangle$ are the eigenstates of $\mathcal{H}^\pm(\mathbf{k})$ with the mirror-rotation symmetry.

It can be proven that the chirality of the second-order Dirac node equals exactly to the difference between the

* These two authors contributed equally.

† anjhong@lzu.edu.cn

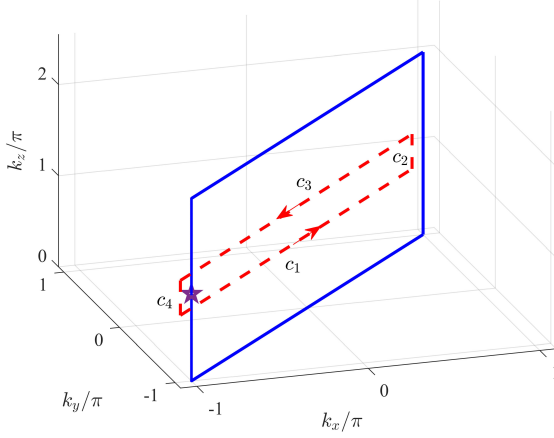


FIG. S1. Closed path (red dashed line) to calculate the chirality of the Dirac points marked by purple star. The blue solid line is the boundary of the Brillouin zone.

mirror-graded winding numbers of the two topological phases separated by this Dirac node. In order to prove this, we choose for convenience a rectangle path depicted in Fig. S1 as c_1 : from $(-\pi - \delta, -\pi - \delta, k_{z,0} - \delta)$ to $(\pi - \delta, \pi - \delta, k_{z,0} - \delta)$, c_2 : from $(\pi - \delta, \pi - \delta, k_{z,0} - \delta)$ to $(\pi - \delta, \pi - \delta, k_{z,0} + \delta)$, c_3 : from $(\pi - \delta, \pi - \delta, k_{z,0} + \delta)$ to $(-\pi - \delta, -\pi - \delta, k_{z,0} + \delta)$, and c_4 : from $(-\pi - \delta, -\pi - \delta, k_{z,0} + \delta)$ to $(-\pi - \delta, -\pi - \delta, k_{z,0} - \delta)$, where δ is an infinitesimal. Then the chirality reads $\mathcal{Q} = \sum_{j=1}^4 \mathcal{Q}_j$ with \mathcal{Q}_j being the chirality contributed by the path c_j . It can be readily

see that \mathcal{Q}_2 and \mathcal{Q}_4 have the same integral function but along opposite integral paths c_2 and c_4 . Thus we have $\mathcal{Q}_2 + \mathcal{Q}_4 = 0$. According to the definition of mirror-graded winding number, we have $\mathcal{Q}_1 = \mathcal{W}(k_{z,0} + \delta)$ and $\mathcal{Q}_3 = -\mathcal{W}(k_{z,0} - \delta)$. Therefore, we obtain $\mathcal{Q} = \mathcal{W}(k_{z,0} + \delta) - \mathcal{W}(k_{z,0} - \delta)$.

To numerically confirm this conclusion, we use Eq. (S5) to calculate the chirality of the Dirac point at $\mathbf{k}_0 = (0, 0, \frac{\pi}{2})$ when $\gamma = -0.2f$ in Fig. 1(b) of the main text. Making the low-energy expansion to $\mathcal{H}^\pm(\theta, k_z)$ near the Dirac node \mathbf{k}_0 , we obtain

$$\mathcal{H}^\pm(\theta, k_z) = \sqrt{2}[-a(k_z - \frac{\pi}{2})\sigma_x \pm \lambda\theta\sigma_y]. \quad (\text{S6})$$

Their eigenstates $|u_\pm(\theta, k_z)\rangle$ corresponding to the respective smaller eigenvalues can be readily calculated. By choosing the closed path c enclosing the Dirac node \mathbf{k}_0 , i.e., $\theta = A \cos \beta$ and $k_z - \frac{\pi}{2} = A \sin \beta$, we can calculate from Eq. (S5)

$$\mathcal{Q}_{\mathbf{k}_0} = \frac{1}{2\pi} \int_0^{2\pi} \frac{a\lambda}{a^2 \sin^2 \beta + \lambda^2 \cos^2 \beta} d\beta = 1. \quad (\text{S7})$$

It is the same as the value calculating from the difference of the mirror-graded winding numbers of its neighboring topological phases, where $\mathcal{W}(k_{z,0} + \delta) = 0$ and $\mathcal{W}(k_{z,0} - \delta) = -1$.

S3. FLOQUET HAMILTONIAN

According to $\Gamma_i \Gamma_j + \Gamma_j \Gamma_i = 2\delta_{ij} I_{4 \times 4}$ and $\Gamma_i^2 = I_{4 \times 4}$, we have $(\mathbf{n} \cdot \mathbf{\Gamma})^2 = n^2 = E^2$ and $e^{-i\alpha \mathbf{n} \cdot \mathbf{\Gamma}} = \cos(\alpha E) - i\mathbf{n} \cdot \mathbf{\Gamma} \sin(\alpha E)$ with $\mathbf{n} = E\mathbf{\hat{n}}$. Therefore, the one-period evolution operator can be expanded as

$$U_T = e^{-i\mathbf{n}_2 \cdot \mathbf{\Gamma} T_2} e^{-i\mathbf{n}_1 \cdot \mathbf{\Gamma} T_1} = \cos(E_1 T_1) \cos(E_2 T_2) - \sin(E_1 T_1) \sin(E_2 T_2) \left[\mathbf{\hat{n}}_1 \cdot \mathbf{\hat{n}}_2 + \sum_{j \neq k}^5 \hat{n}_{1j} \hat{n}_{2k} \Gamma_j \Gamma_k \right] - i\mathbf{\hat{n}}_1 \cdot \mathbf{\Gamma} \sin(E_1 T_1) \cos(E_2 T_2) - i\mathbf{\hat{n}}_2 \cdot \mathbf{\Gamma} \cos(E_1 T_1) \sin(E_2 T_2) \equiv A I_{4 \times 4} - iB, \quad (\text{S8})$$

where A and B are

$$A = \cos(E_1 T_1) \cos(E_2 T_2) - \sin(E_1 T_1) \sin(E_2 T_2) \mathbf{\hat{n}}_1 \cdot \mathbf{\hat{n}}_2, \quad (\text{S9})$$

$$B = -i \sin(E_1 T_1) \sin(E_2 T_2) \sum_{j \neq k}^5 \hat{n}_{1j} \hat{n}_{2k} \Gamma_j \Gamma_k + \mathbf{\hat{n}}_1 \cdot \mathbf{\Gamma} \sin(E_1 T_1) \cos(E_2 T_2) + \mathbf{\hat{n}}_2 \cdot \mathbf{\Gamma} \cos(E_1 T_1) \sin(E_2 T_2). \quad (\text{S10})$$

The unitariness of U_T requires that $A^2 I_{4 \times 4} + B^2 = I_{4 \times 4}$. It indicates that $B^2 = \mathcal{B}^2 I_{4 \times 4}$ and $A^2 + \mathcal{B}^2 = 1$. Thus we have

$$U_T = \cos(\arccos A) I_{4 \times 4} - i \frac{B}{\mathcal{B}} \sin(\arccos A) = \exp \left[-i \frac{B}{\mathcal{B}} \arccos A \right]. \quad (\text{S11})$$

Then according to $\mathcal{H}_{\text{eff}} = \frac{i}{T} \ln U_T$, the effective Hamiltonian reads

$$\mathcal{H}_{\text{eff}} = \frac{\arccos A}{T} \frac{B}{\mathcal{B}}. \quad (\text{S12})$$

Using the fact that the eigenvalues of B are $\pm \mathcal{B}$, we readily obtain the eigenvalues of \mathcal{H}_{eff} are

$$\varepsilon = \pm \frac{\arccos A}{T}. \quad (\text{S13})$$

When $A = 1$, the band touching point occurs at $\varepsilon = 0$. When $A = -1$, the band touching point occurs at $\varepsilon = \pi/T$. According to Eq. (S9), the bands touch at $\varepsilon = 0$ for the points of \mathbf{k} and driving parameters which satisfy either

$$T_j E_j = z_j \pi, \quad (\text{S14})$$

$$\text{or } \begin{cases} \mathbf{n}_1 \cdot \mathbf{n}_2 = \pm 1 \\ T_1 E_1 \pm T_2 E_2 = z\pi, \end{cases} \quad (\text{S15})$$

where z_1 and z_2 are integers with same parity, and z is even number. The bands touch at $\varepsilon = \pi/T$ for the points of \mathbf{k} and the driving parameters which satisfy either

$$T_j E_j = z_j \pi, \quad (\text{S16})$$

$$\text{or } \begin{cases} \mathbf{n}_1 \cdot \mathbf{n}_2 = \pm 1 \\ T_1 E_1 \pm T_2 E_2 = z\pi, \end{cases} \quad (\text{S17})$$

where z_1 and z_2 are integers with different parities, and z is odd number.

S4. SYMMETRY ANALYSIS

It can be verified that the static Hamiltonian (1) in the main text possesses the time-reversal symmetry $\mathcal{T}\mathcal{H}_j(\mathbf{k})\mathcal{T}^{-1} = \mathcal{H}_j^*(\mathbf{k}) = \mathcal{H}_j(-\mathbf{k})$, the chiral symmetry $\mathcal{S}\mathcal{H}_j(\mathbf{k}) = -\mathcal{H}_j(\mathbf{k})$, the inversion symmetry $\mathcal{P}\mathcal{H}_j(\mathbf{k})\mathcal{P}^{-1} = \mathcal{H}_j(-\mathbf{k})$, and the mirror-rotation symmetry $\mathcal{M}_{xy}\mathcal{H}_j(\mathbf{k})\mathcal{M}_{xy}^{-1} = \mathcal{H}_j(k_y, k_x, k_z)$. It can be proven that the latter two symmetries are preserved, while the former two symmetries are broken by our periodic driving. According to $\mathcal{H}_{\text{eff}}(\mathbf{k}) \equiv \frac{i}{T} \ln U_T(\mathbf{k})$ and $U_T(\mathbf{k}) = e^{-i\mathcal{H}_2(\mathbf{k})T_2} e^{-i\mathcal{H}_1(\mathbf{k})T_1}$, we have

$$\begin{aligned} \mathcal{P}U_T(\mathbf{k})\mathcal{P}^{-1} &= e^{-i\mathcal{H}_2(-\mathbf{k})T_2} e^{-i\mathcal{H}_1(-\mathbf{k})T_1} \\ &= U_T(-\mathbf{k}), \end{aligned} \quad (\text{S18})$$

$$\begin{aligned} \mathcal{M}_{xy}U_T(\mathbf{k})\mathcal{M}_{xy}^{-1} &= e^{-i\mathcal{H}_2(k_y, k_x, k_z)T_2} e^{-i\mathcal{H}_1(k_y, k_x, k_z)T_1} \\ &= U_T(k_y, k_x, k_z), \end{aligned} \quad (\text{S19})$$

which results in that the inversion and mirror-rotation symmetries are inherited by $\mathcal{H}_{\text{eff}}(\mathbf{k})$. On the other hand, because

$$\mathcal{T}U_T(\mathbf{k})\mathcal{T}^{-1} = e^{i\mathcal{H}_2(-\mathbf{k})T_2} e^{i\mathcal{H}_1(-\mathbf{k})T_1} \neq U_T^\dagger(-\mathbf{k}), \quad (\text{S20})$$

$$\mathcal{S}U_T(\mathbf{k})\mathcal{S}^{-1} = e^{i\mathcal{H}_2(\mathbf{k})T_2} e^{i\mathcal{H}_1(\mathbf{k})T_1} \neq U_T^{-1}(\mathbf{k}), \quad (\text{S21})$$

the time-reversal and chiral symmetries are broken by $\mathcal{H}_{\text{eff}}(\mathbf{k})$.

However, the time-reversal and chiral symmetries can be simultaneously recovered by the unitary transformation $G_1(\mathbf{k}) = e^{-i\mathcal{H}_1(\mathbf{k})T_1/2}$ and $G_2(\mathbf{k}) = e^{i\mathcal{H}_2(\mathbf{k})T_2/2}$. Using $\tilde{\mathcal{H}}_{\text{eff},j}(\mathbf{k}) = \frac{i}{T} \ln \tilde{U}_{T,j}(\mathbf{k})$ with $\tilde{U}_{T,j}(\mathbf{k}) = G_j(\mathbf{k})U_T(\mathbf{k})G_j^{-1}(\mathbf{k})$, we have

$$\begin{aligned} \mathcal{T}\tilde{U}_{T,1}(\mathbf{k})\mathcal{T}^{-1} &= e^{i\mathcal{H}_1(-\mathbf{k})T_1/2} e^{i\mathcal{H}_2(-\mathbf{k})T_2} e^{i\mathcal{H}_1(-\mathbf{k})T_1/2} \\ &= \tilde{U}_{T,1}^\dagger(-\mathbf{k}), \end{aligned} \quad (\text{S22})$$

$$\begin{aligned} \mathcal{T}\tilde{U}_{T,2}(\mathbf{k})\mathcal{T}^{-1} &= e^{i\mathcal{H}_2(-\mathbf{k})T_2/2} e^{i\mathcal{H}_1(-\mathbf{k})T_1} e^{i\mathcal{H}_2(-\mathbf{k})T_2/2} \\ &= \tilde{U}_{T,2}^\dagger(-\mathbf{k}), \end{aligned} \quad (\text{S23})$$

which means that the time-reversal symmetry $\mathcal{T}\tilde{\mathcal{H}}_{\text{eff},j}(\mathbf{k})\mathcal{T}^{-1} = \tilde{\mathcal{H}}_{\text{eff},j}(-\mathbf{k})$ is recovered in $\tilde{\mathcal{H}}_{\text{eff},j}(\mathbf{k})$. In the similar manner, we can prove

$$\begin{aligned} \mathcal{S}\tilde{U}_{T,1}(\mathbf{k})\mathcal{S}^{-1} &= e^{i\mathcal{H}_1(\mathbf{k})T_1/2} e^{i\mathcal{H}_2(\mathbf{k})T_2} e^{i\mathcal{H}_1(\mathbf{k})T_1/2} \\ &= \tilde{U}_{T,1}^{-1}(\mathbf{k}), \end{aligned} \quad (\text{S24})$$

$$\begin{aligned} \mathcal{S}\tilde{U}_{T,2}(\mathbf{k})\mathcal{S}^{-1} &= e^{i\mathcal{H}_2(\mathbf{k})T_2/2} e^{i\mathcal{H}_1(\mathbf{k})T_1} e^{i\mathcal{H}_2(\mathbf{k})T_2/2} \\ &= \tilde{U}_{T,2}^{-1}(\mathbf{k}), \end{aligned} \quad (\text{S25})$$

which means that the chiral symmetry $\mathcal{S}\tilde{\mathcal{H}}_{\text{eff},j}(\mathbf{k})\mathcal{S}^{-1} = -\tilde{\mathcal{H}}_{\text{eff},j}(\mathbf{k})$ is also recovered in $\tilde{\mathcal{H}}_{\text{eff},j}(\mathbf{k})$. With these two symmetries recovered, we can use the similar way as the static system to establish the bulk-corner correspondence by defining the proper topological invariants for our periodically driven system.

It is interesting to note that the original effective Hamiltonian $\mathcal{H}_{\text{eff}}(\mathbf{k})$ equivalently possesses a hidden time-reversal symmetry and a hidden chiral symmetry after performing the inverse unitary transformations. After rewriting Eqs. (S22) and (S23) as

$$\mathcal{T}G_j(\mathbf{k})U_T(\mathbf{k})G_j^{-1}(\mathbf{k})\mathcal{T}^{-1} = G_j(-\mathbf{k})U_T^\dagger(-\mathbf{k})G_j^{-1}(-\mathbf{k}), \quad (\text{S26})$$

we readily obtain

$$G_j^{-1}(-\mathbf{k})\mathcal{T}G_j(\mathbf{k})U_T(\mathbf{k})G_j^{-1}(\mathbf{k})\mathcal{T}^{-1}G_j(-\mathbf{k}) = U_T^\dagger(-\mathbf{k}). \quad (\text{S27})$$

It implies that the original effective $\mathcal{H}_{\text{eff}}(\mathbf{k})$ possesses the time-reversal symmetry under the newly defined time-reversal operator $G_j^{-1}(-\mathbf{k})\mathcal{T}G_j(\mathbf{k})$. Similarly, Eqs. (S24) and (S25) result in

$$G_j^{-1}(\mathbf{k})\mathcal{S}G_j(\mathbf{k})U_T(\mathbf{k})G_j^{-1}(\mathbf{k})\mathcal{S}^{-1}G_j(\mathbf{k}) = U_T^{-1}(\mathbf{k}). \quad (\text{S28})$$

It implies that $\mathcal{H}_{\text{eff}}(\mathbf{k})$ possesses the chiral symmetry under the newly defined chiral operator $G_j^{-1}(\mathbf{k})\mathcal{S}G_j(\mathbf{k})$.

S5. WEYL NODES

The Hamiltonian along the high-symmetry lines $k_x = k_y = \theta = 0$ or π satisfies $[\mathcal{H}_1(\theta, k_z) + ip\Gamma_1\Gamma_3, \mathcal{H}_2(\theta, k_z) + ip\Gamma_1\Gamma_3] = 0$. Thus we have

$$\begin{aligned} \mathcal{H}_{\text{eff}}(\theta, k_z) &= \sum_{j=1,2} [\gamma_j + \chi(k_z) \cos \theta] (\Gamma_5 - \Gamma_2) T_j / T \\ &\quad + ip\Gamma_1\Gamma_3 (T_1 + T_2) / T. \end{aligned} \quad (\text{S29})$$

Its eigenvalues are $\pm \varepsilon_{\pm}(\theta, k_z)$, where

$$\begin{aligned} \varepsilon_{\pm}(\theta, k_z) &= p(T_1 + T_2) / T \pm \sqrt{2} |\gamma_1 T_1 + \gamma_2 T_2 \\ &\quad + e^{i\theta} \chi(k_z) (T_1 + T_2) / T|. \end{aligned} \quad (\text{S30})$$

The Weyl points are present if

$$\varepsilon_{\pm}(\theta, k_z) = n_{\theta, \pm} \pi / T. \quad (\text{S31})$$

We plot in Fig. S2 the four quasienergies $\pm \varepsilon_{\pm}(\theta, k_z)$ along the high-symmetry line $\theta = 0$ and π . They explain

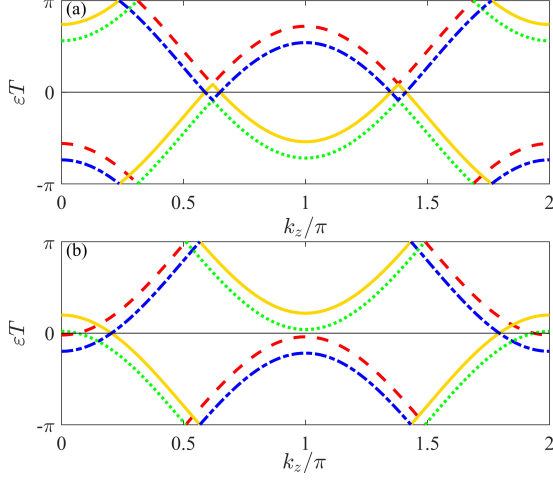


FIG. S2. Quasienergies $\pm\epsilon_{\pm}(\theta, k_z)$ with $\theta = 0$ (a) and π (b) of $\mathcal{H}_{\text{eff}}(\theta, k_z)$. We use the parameters same as Fig. 4 in the main text.

well the Weyl points formed in Fig. 4(a) of the main text. The Weyl points at $k_z = 0.06\pi$ and 0.51π are reproduced by Eq. (S31) with $n_{\pi,+} = 2$ and 3, respectively. The ones at $k_z = 0.21\pi$ and 0.57π are reproduced by Eq. (S31) with $n_{\pi,-} = -2$ and -3 , respectively. The ones at $k_z = 0.24\pi$ and 0.59π are reproduced by Eq. (S31) with $n_{0,-} = -1$ and 0, respectively. The ones $k_z = 0.31\pi$ and 0.65π are reproduced by Eq. (S31) with $n_{0,+} = 1$ and $n_{0,-} = 0$, respectively.

S6. WILSON LOOP

The Chern insulator is characterized by the Chern number. The Chern number relates to the Wannier center $\frac{-i}{2\pi} \log[W(k_y, k_z)]$ as [5]

$$\mathcal{C}(k_z) = \frac{-i}{2\pi} \int_0^{2\pi} \partial_{k_y} \log[W(k_y, k_z)] dk_y, \quad (\text{S32})$$

where $W(k_y, k_z)$ is called Wilson loop. The Wilson loop is defined by the multiplication of the discretized Berry connections along k_x , i.e.

$$W(k_y, k_z) = \prod_{j=0}^{N-1} \langle u(k_x + (j+1)\Delta, k_y, k_z) | u(k_x + j\Delta, k_y, k_z) \rangle \quad (\text{S33})$$

where $|u(k_x, k_y, k_z)\rangle$ is the eigen state of $\mathcal{H}_{\text{eff}}(\mathbf{k})$ and $\Delta = 2\pi/N$. The Wannier center itself can also act as a quantification of the topological phase. If the Wannier center $\frac{-i}{2\pi} \log[W(k_y, k_z)]$ changes from -0.5 to 0.5 when k_y runs over the full Brillouin zone, then the system is a Chern insulator with one pair of chiral boundary state formed.

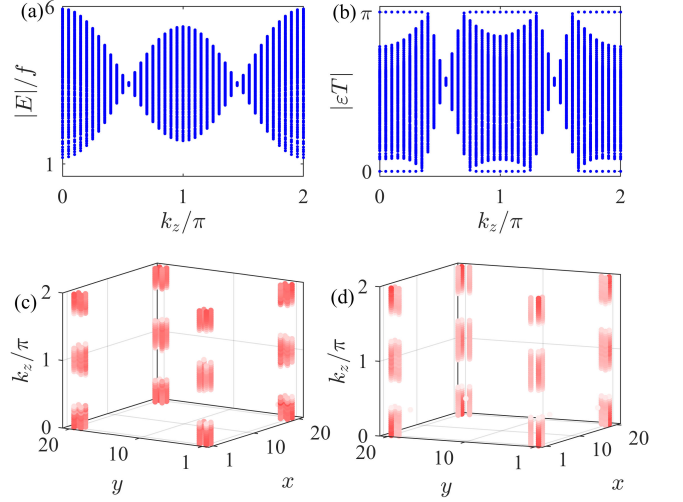


FIG. S3. (a) Energy spectrum of the static systems H_1 and H_2 under the open-boundary condition along x and y directions. (b) Quasienergy spectrum of the periodically changed system between H_1 and H_2 under the open-boundary condition along x and y directions. Hinge Fermi arcs of the zero modes in (c) and the π/T mode in (d). The parameters are $T_1 = 0.5f^{-1}$, $T_2 = f^{-1}$, $a = 1.5f$, $\lambda = 0.2f$, and $q_2 = q_1 = -2.5$.

S7. CONVERSION OF DIFFERENT ORDERS OF SEMIMETALS

The periodic driving also possesses the ability to realize the inter-conversion of different orders of topological semimetals. More interesting, not only the second-order topological semimetal from the static first-order semimetal, but also the one from the static normal insulator can be realized by the periodic driving.

Figure S3 shows the result that a second-order Dirac semimetal is produced from the static normal insulator by the periodic driving. The energy spectrum of the static Hamiltonian H_1 in Fig. S3(a), which is the same as the one of H_2 , indicates that there is no band touching point and thus both of H_1 and H_2 are topologically trivial. When H_1 and H_2 are periodically inter-changed under the protocol (2) in the main text, a series of Dirac nodal points and zero- and π/T -mode bound states are formed in the quasienergy spectrum [see Fig. S3(b)]. The corresponding probability distributions of the zero- and π/T -mode bound states in Figs. S3(c) and S3(d) signify the presence of the hinge Fermi arcs. It confirms the second-order nature of the formed Dirac nodal points in Fig. S3(b). Therefore, we succeed in converting the static normal insulator to a second-order Dirac semimetal by our periodic driving protocol.

Figure S3 shows the result that a second-order Weyl semimetal is produced from the static first-order Weyl semimetal by the periodic driving. The energy spectrum of the static system H_1 in Fig. S3(a), which is the same as the one of H_2 , reveals three continuous band touching lines. The 2D Chern insulators characterized by the gap-

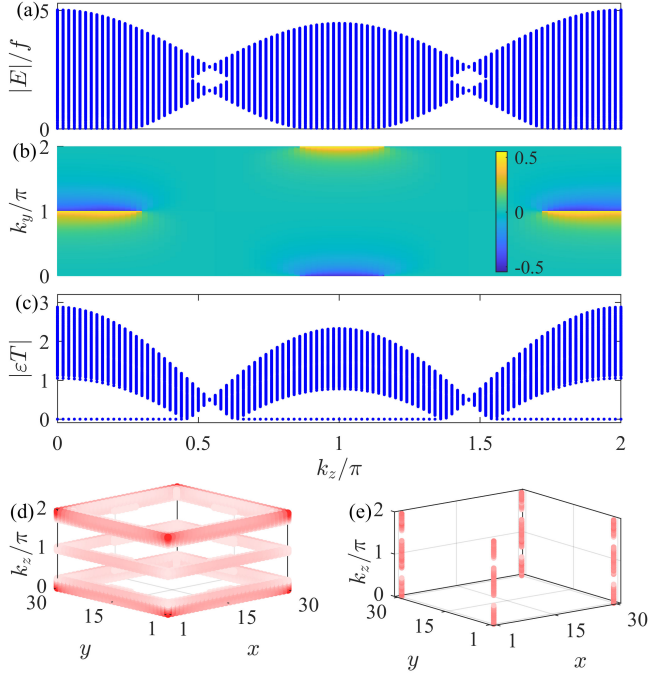


FIG. S4. (a) Energy spectrum under the open-boundary condition along x and y directions and (b) Wannier centers for the zero mode of the static systems H_1 and H_2 . (c) Quasienergy spectrum of the periodically changed system between H_1 and H_2 under the open-boundary condition along x and y directions. Surface Fermi arcs of the zero modes corresponding to the static systems H_1 and H_2 in (d). Hinge Fermi arcs of the zero modes corresponding to the periodically driven system in (e). The parameters are $T_1 = T_2 = 0.5f^{-1}$, $a = 1.5f$, $\lambda = 0.2f$, $p = 0.5f$, and $q_2 = -q_1 = 1.5$.

less chiral boundary states are formed within these band touching lines. They can be topologically witnessed by the Wannier center in Fig. S4(b), where the jump of the Wannier center from -0.5 to 0.5 when k_y runs from 0 to 2π verifies the formation of a first-order Chern band. The probability distribution of the gapless chiral boundary states contributes to the surface Fermi arcs [see Fig. S3(d)]. It demonstrates that both of the static systems H_1 and H_2 are the first-order Weyl semimetal, which is sliced into a family of 2D Chern insulators and normal insulators separated by the Weyl points. When H_1 and H_2 are periodically inter-changed under the protocol (2) in the main text, it is interesting to find from the quasienergy spectrum in Fig. S4(c) that a series of 2D zero-mode corner states are formed. The probability distributions of these corner states form the hinge Fermi arcs [see Fig. S3(e)]. Thus, the periodically driven system is a second-order Weyl semimetal. By this example, we succeed in converting the static first-order Weyl semimetal to a second-order one by the periodic driving.

-
- [1] W. A. Benalcazar, B. A. Bernevig, and T. L. Hughes, Quantized electric multipole insulators, *Science* **357**, 61 (2017).
 - [2] W. A. Benalcazar, B. A. Bernevig, and T. L. Hughes, Electric multipole moments, topological multipole moment pumping, and chiral hinge states in crystalline insulators, *Phys. Rev. B* **96**, 245115 (2017).
 - [3] S. Imhof, C. Berger, F. Bayer, J. Brehm, L. W. Molenkamp, T. Kiessling, F. Schindler, C. H. Lee, M. Greiter, T. Neupert, and R. Thomale, Topoelectrical-circuit realization of topological corner modes, *Nature Physics* **14**, 925 (2018).
 - [4] A. A. Burkov, M. D. Hook, and L. Balents, Topological nodal semimetals, *Phys. Rev. B* **84**, 235126 (2011).
 - [5] H.-X. Wang, Z.-K. Lin, B. Jiang, G.-Y. Guo, and J.-H. Jiang, Higher-order Weyl semimetals, *Phys. Rev. Lett.* **125**, 146401 (2020).